X-ray spectra in the magnetic van der Waals materials math xmlns="http://www.w3.org/1998/Math/MathML">mrow>msub>mi>Fe/mi>mn>3/mn>/msub>mi>Ge/mi>msub>mi>Te/mi>mn>2/mn>/msub>mo>,/mo>/mrow>/math> math xmlns="http://www.w3.org/1998/Math/MathML">mrow>msub>mi>CrI/mi>mn>3/mn>/msub>mo>,/mo>/mrow>mo> /mo>mi>and/mi>mo> /mo>mrow>mi>Cr/mi>mi>Ge/mi>msub>mi>Te/mi>mn>3/mn>/msub>/mrow>/math>: A first-principles study

Y. Lee, V. N. Antonov, B. N. Harmon, and Liqin Ke

Phys. Rev. B **103**, 134407 — Published 6 April 2021

DOI: 10.1103/PhysRevB.103.134407

X-ray spectra in magnetic van der Waals materials Fe_3GeTe_2, CrI_3, and $CrGeTe_3$: a first-principles study

Y. Lee,[1] V. N. Antonov,[2] B. N. Harmon,[1] and Liqin Ke[1]

[1] *Ames Laboratory, U.S. Department of Energy, Ames, Iowa 50011*
[2] *G. V. Kurdyumov Institute for Metal Physics of the N.A.S. of Ukraine, 36 Academician Vernadsky Boulevard, UA-03142 Kyiv, Ukraine*

(Dated: March 16, 2021)

Using density functional theory (DFT) methods, we have calculated X-ray absorption spectroscopy (XAS) and X-ray circular dichroism (XMCD) spectra in bulk and thin films of Fe_3GeTe_2, CrI_3, and $CrGeTe_3$. DFT+U methods are employed for better handling of correlation effects of $3d$ electrons of transition metals. We discuss relations between the density of states, radial matrix elements, and the corresponding spectra. By comparing the calculated spectra with previously measured spectra, we discuss the reliability of DFT+U methods to describe the electronic structures of these materials and determine the corresponding optimal U and J parameters.

I. INTRODUCTION

Graphene is an attractive material because of its novel electronic structure and its potential for practical applications [1–4]. However, the lack of intrinsic magnetism is a limitation for some device applications. Nevertheless, considerable effort has been expended to induce and control magnetism in graphene [5, 6] and separately to discover new two-dimensional (2D) materials that have intrinsic magnetism. Recent unprecedented experimental realization of magnetic 2D van der Waals (vdW) materials [7, 8] has created great excitement and determination to explore magnetism in these new 2D materials.

Among the magnetic 2D vdW (m2DvdW) materials, CrI_3, $CrGeTe_3$ and Fe_3GeTe_2 are the most intensively investigated ferromagnetic materials to understand fundamental physics such as the mechanism of magnetic ordering, the exchange interaction and the magnetocrystalline anisotropy as well as to improve desired properties by controlling external conditions such as electric and magnetic fields, strain, pressure, and doping [9–17]. Furthermore, since it is easy to separate vdW materials into thin layers and to over-lay different materials, the creation and exploration of composite thin layers has expanded the study of a wide variety of new interfaces and composite layered materials [18–24].

To investigate magnetic properties of heterostructures and alloys consisting of different magnetic atoms, it is beneficial to separate contributions from different atoms instead of averaging or summing them. X-ray Magnetic Circular Dichroism (XMCD) is useful for understanding the roles of individual magnetic atoms responsible for collective magnetic properties such as the magnetic ordering in interfaces of heterostructures. For instance, Liu *et al.* [25] performed XMCD measurements on a superlattice structure of Fe_3GeTe_2 and CrSb; and discovered that T_C of Fe_3GeTe_2 can be significantly enhanced because of the interfacial ferromagnetic coupling. Also, Burn *et al.* [26] were able to characterize magnetic properties of the layers of Cr_2Te_3 thin films and Cr_2Te_3/Cr:Sb_2Te_3 (Cr doped Sb_2Te_3) heterostructures by XMCD measurements.

X-ray absorption spectroscopy (XAS) and XMCD have become essential tools for investigating magnetic properties of ferromagnetic alloys, surfaces and interfaces as well as magnetic bulk compounds because of the chemical and orbital selectivity of X-ray spectra [27–31]. These tools are able to resolve the total magnetic moment into the orbital and spin contributions by using sum rules. And they can assess magnetic information of each element within compounds and interfacial structures. Moreover, since these techniques involve electron transitions from well defined core states to (at times complex) conduction states, the spectra provide knowledge of the composition of the density of states (DOS) and the orbital character of the conduction bands.

Since the magnetic moment is a number that involves integration, it is not easy to pinpoint the origin or details of any differences of states by comparing their magnetic moments. On the other hand a comparison of DOSs can give information about the differences. In the experiment, optical spectra give energy-resolved information and can be compared with DOS(E). In XAS/XMCD, since initial states are well defined atomic core states, which are not affected by surroundings, it is useful to obtain information of final conduction states. Comparison of theoretical spectra which are calculated with various methods and experimental XAS/XMCD spectra help to decide the more suitable theoretical method for further work. It is possible to associate key structures of spectra with calculated DOS and obtain electronic structure information.

There are a number of reports for XMCD measurements for bulk m2DvdW materials such as Fe_3GeTe_2 [32, 33], CrI_3 [34, 35] and $CrGeTe_3$ [36]. For Fe_3GeTe_2, the XAS and XMCD spectra of Fe $L_{3,2}$ edges have been measured [32, 33]. Zhu *et al.* [32] extracted the orbital moment of Fe atoms from the spectra and found good agreement with their calculations and Park *et al.* [33] showed that the ratio between orbital and spin moments of Fe atoms (~ 0.092) in Fe_3GeTe_2 is much higher than in elemental Fe ($\sim$0.04). Li *et al.*[37] measured

the temperature-dependent XMCD spectra to study the magnetic ordering of Fe_3GeTe_2 and found a T_C of 230 K, which agrees with the SQUID result.

For CrI_3, Frisk *et al.* [34] measured the Cr $L_{3,2}$ edges spectra and calculated the spectra using atomic multiplet theory [38]. Using XMCD spectra, Kim *et al.* [35] estimated in-plane and out-of-plane orbital moments (m_l) and concluded that the anisotropy of magnetic orbital moments in CrI_3 is negligible, unlike in $CrGeTe_3$. For $CrGeTe_3$, Waston *et al.* [36] performed XAS and XMCD measurements and atomic multiplet calculations for the Cr $L_{3,2}$ edges spectra of $CrGeTe_3$. Along with angle-resolved photoemission spectroscopy (ARPES) measurements, they identified covalent bonding states and suggested these states as the primary driver of the ferromagnetic ordering of $CrGeTe_3$.

Most theoretical studies of the X-ray spectra in m2DvdW materials so far were based on atomic multiplet theory or cluster models [39], which employ adjustable parameters to describe the electronic structure and X-ray spectra. Though the reported theoretical spectral line shapes may show good agreement with experiments, it is hard to interpret the electronic structure in a comprehensive way because they rely on selected parameters. Atomic multiplet theory allows an easy incorporation of many-body effects but is not reliable for interpreting solid-state-like effects. Therefore, solid state first-principles calculations are useful for an integrated understanding of the system while the atomic and empirical approaches provide complementary information.

In this study, we calculate and discuss the electronic structure and X-ray spectra of Fe_3GeTe_2, CrI_3, and $CrGeTe_3$. We performed calculations not only with bulk structures but also with thin-film structures since most of reported X-ray spectra measurements [32, 34, 35] were done in total-electron-yield (TEY) mode which is surface sensitive and the probing depth of TEY is about 3-10 *nm*, depending on materials [39]. Since the *c*-lattice parameter is about or less than 2 *nm* , X-ray spectra in TEY mode may not yield bulk structure information for CrI_3, $CrGeTe_3$ and Fe_3GeTe_2. Furthermore, the m2DvdW are attractive because of their thin-layer character. Therefore, it is interesting to investigate the X-ray spectra of thin films (layers). We show that X-ray spectra are useful for determining the unoccupied DOS through comparison between the partial DOSs and spectral line shape. Electronic structures are described within density functional theory (DFT) and DFT+U. By comparison between the theoretical and experimental spectra, we determine the optimal U and J values that are able to describe the electronic structures of these materials more satisfactorily within the DFT+U framework.

II. THEORY AND COMPUTATIONAL DETAILS

A. X-ray magnetic circular dichroism.

Magneto-optical (MO) effects refer to various changes in the polarization state of light upon interaction with materials possessing a net magnetic moment, including rotation of the plane of linearly polarized light (Faraday, Kerr rotation), and the complementary differential absorption of left and right circularly polarized light (circular dichroism). In the near visible spectral range these effects result from excitation of electrons in the conduction band. Near x-ray absorption edges, or resonances, magneto-optical effects can be enhanced by transitions from well-defined atomic core levels to empty valence or conduction states.

Within the one-particle approximation, the absorption coefficient $\mu_j^\lambda(\omega)$ for incident x-ray polarization λ and photon energy $\hbar\omega$ can be determined as the probability of electronic transitions from initial core states with the total angular momentum j to final unoccupied Bloch states

$$\mu_j^\lambda(\omega) = \sum_{m_j}\sum_{n\mathbf{k}} |\langle\Psi_{n\mathbf{k}}|\Pi_\lambda|\Psi_{jm_j}\rangle|^2 \delta(E_{n\mathbf{k}} - E_{jm_j} - \hbar\omega) \times\theta(E_{n\mathbf{k}} - E_F)\,, \quad (1)$$

where Ψ_{jm_j} and E_{jm_j} are the wave function and the energy of a core state with the projection of the total angular momentum m_j; $\Psi_{n\mathbf{k}}$ and $E_{n\mathbf{k}}$ are the wave function and the energy of a valence state in the n-th band with the wave vector $\mathbf{k}$; E_F is the Fermi energy.

Π_λ is the electron-photon interaction operator in the dipole approximation

$$\Pi_\lambda = -e\boldsymbol{\alpha}\mathbf{a}_\lambda, \quad (2)$$

where $\boldsymbol{\alpha}$ are the Dirac matrices and $\mathbf{a}_\lambda$ is the λ polarization unit vector of the photon vector potential, with $a_\pm = 1/\sqrt{2}(1, \pm i, 0)$, $a_\parallel = (0, 0, 1)$. Here, + and − denote, respectively, left and right circular photon polarization with respect to the magnetization direction in the solid. Then, x-ray magnetic circular and linear dichroism are given by $\mu_+ - \mu_-$ and $\mu_\parallel - (\mu_+ + \mu_-)/2$, respectively. More detailed expressions of the matrix elements in the electric dipole approximation in the frame of the fully relativistic Dirac LMTO method may be found in Ref. [40].

Concurrent with the development of x-ray magnetic circular dichroism experiments, some important magneto-optical sum rules have been derived [41–44].

For the $L_{2,3}$ edges the l_z sum rule can be written as [40]

$$\langle l_z\rangle = n_h \frac{4\int_{L_3+L_2} d\omega(\mu_+ - \mu_-)}{3\int_{L_3+L_2} d\omega(\mu_+ + \mu_-)} \quad (3)$$

where n_h is the number of holes in the d band $n_h = 10 - n_d$, $\langle l_z\rangle$ is the average of the magnetic quantum number

of the orbital angular momentum. The integration is taken over the whole $2p$ absorption region. The s_z sum rule can be written as

$$\langle s_z\rangle + \frac{7}{2}\langle t_z\rangle = n_h \frac{\int_{L_3} d\omega(\mu_+ - \mu_-) - 2\int_{L_2} d\omega(\mu_+ - \mu_-)}{\int_{L_3+L_2} d\omega(\mu_+ + \mu_-)} \quad (4)$$

where t_z is the z component of the magnetic dipole operator $\mathbf{t} = \mathbf{s} - 3\mathbf{r}(\mathbf{r}\cdot\mathbf{s})/|\mathbf{r}|^2$ which accounts for the asphericity of the spin moment. The integration $\int_{L_3}$ ($\int_{L_2}$) is taken only over the $2p_{3/2}$ ($2p_{1/2}$) absorption region.

B. Computational details

The X-ray spectra [45] are calculated using the eigenvalues and wavefunctions of self-consistent electronic structures calculations, which are carried out within DFT or DFT+U using a full-potential linear augmented plane wave (FLAPW) method [46] as well as the fully relativistic linear muffin-tin orbital (RLMTO) method [47, 48]. This implementation of the LMTO method uses four-component basis functions constructed by solving the Dirac equation inside an atomic sphere [49]. The generalized gradient approximation (GGA) [50] was used for the correlation and exchange potentials. As for DFT+U, we use both the fully-localized-limit (FLL) [51, 52] and around-the-mean-field (AMF) [53] double-counting schemes with correlation parameters U and J applied on the cation-3d orbitals. We also used in this work the "relativistic" generalization of the rotationally invariant version of the LSDA+U method (RG) [54] which takes into account SO coupling so that the occupation matrix of localized electrons becomes non-diagonal in spin indices.

In the x-ray absorption process an electron is promoted from a core level to an unoccupied state, leaving a core hole. As a result, the electronic structure at this state differs from that of the ground state. In order to reproduce the experimental spectrum the self-consistent calculations should be carried out including a core hole. In this study the core-hole effect was fully taken into account in the self-consistent iterations by removing an electron at the core orbital using the supercell approximation. The core state of the target atom in the ground state provides the initial state $|i>$ for the spectral calculation. The final states $|f>$ are the conduction band states obtained separately by the calculations in which one of the core electrons of the target atom is placed at the lowest conduction band. The interaction and the screening of the electron-hole pair are fully accounted for by the self-consistent iterations of the final state Kohn-Sham equations. This procedure simulates the experimental situation, in which the sample can easily supply an electron to screen a localized charge produced by the core hole. Such an approach considers the symmetry breaking of the system in a natural way, and self-consistently describes the charge redistribution induced by the core hole.

We employed the experimental lattice parameters [55–57] for calculations. We used hexagonal cells which have six formula units, with three layers instead of rhombohedral primitive cells for CrI_3 and $CrGeTe_3$. For the thin film calculations, we took one unit cell of hexagonal structures for CrI_3, $CrGeTe_3$ and a 1×1×2 supercell for Fe_3GeTe_2 and added a 25 *a.u.* vacuum region. In all of the bulk and film calculations, we did not perform any structural optimization calculations.

III. RESULTS & DISCUSSION

A. Fe_3GeTe_2

1. *Electronic structure*

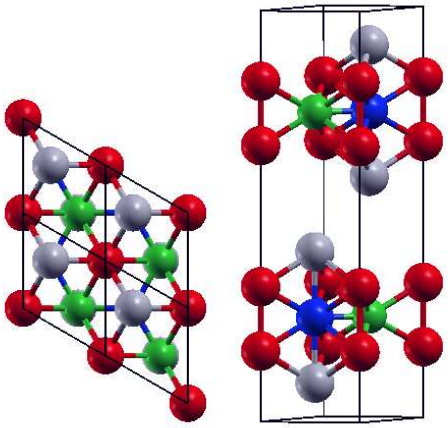

FIG. 1. Schematic crystal structure of Fe_3GeTe_2. The Fe_1 atoms are red, Fe_2 atoms are blue, the Ge atoms are green and the Te atoms are gray. The top view (left) shows a 2×2×1 supercell and the side view (right) shows a primitive unit cell. We used Xcrysden [58] for generating the structure figure.

Fe_3GeTe_2 crystallizes in a hexagonal ($P63/mmc$, space group no. 194) structure [57, 59]. The primitive cell contains two formula units (f.u.). As shown in Fig. 1, a Te atom occupies the $4f(3m)$ site and a Ge atom occupies the $2d(-6m2)$ site, while Fe atoms are divided into two sublattices, $4e(3m)$ and $2c(-6m2)$, denoted as Fe_1 and Fe_2, respectively. Each sublattice forms a trigonal lattice in the basal plane. Fe_2 and Ge atoms, together, form a Fe_2-Ge honeycomb monolayer; sandwiched between two Te-capped Fe_1 layers. The nearest neighbor of an Fe_1 atom is an Fe_1 atom along the z direction and their distance is 2.554 Å, and the distance between Fe_2 and its nearest neighbor Ge is 2.304 Å.

Figure 2 presents the partial density of states of Fe_3GeTe_2 in the GGA approximation. The contribution of the Te 5s states consists of two peaks that are located

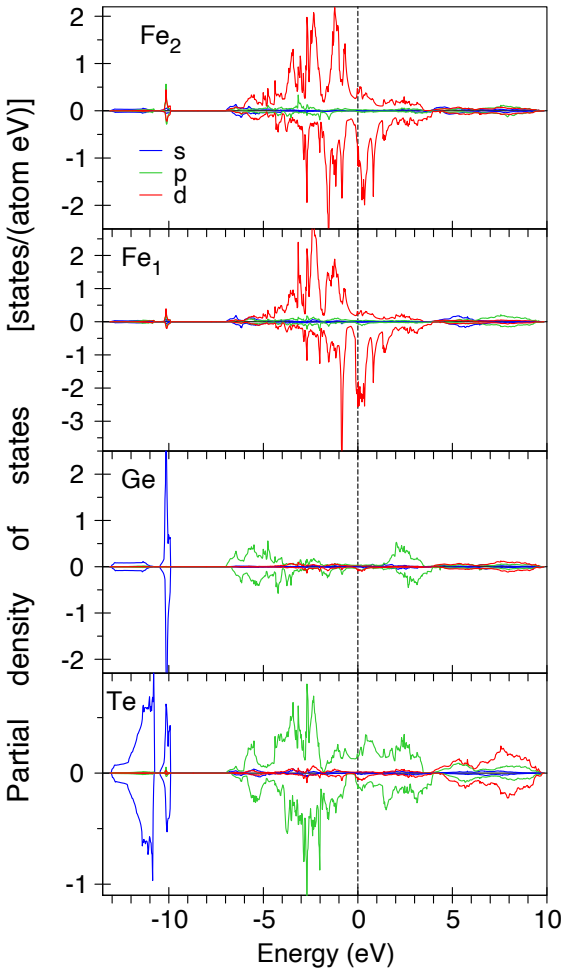

FIG. 2. The partial DOSs of bulk Fe_3GeTe_2 calculated in the GGA approximation. Positive (Negative) DOS are up (down) spin states.

mostly between −13.1 and −10.8 eV below the Fermi level. The second double peak located between −10.5 and −9.7 eV originates from the hybridization with Ge 4*s* states. The Ge 4*s* bands are located mostly between −10.5 and −9.9 eV. The low intensity wide fine structure situated between −13.1 and −10.8 eV is due the hybridization with Te 5*s* states. The 5*p* states of Te are found to be in the −7 eV to 3.5 eV energy interval. The 4*p* states of Ge occupy the same energy interval, although, they have relatively small intensity in the vicinity of the Fermi level. The spin splittings of the Te and Ge *p* states are quite small. The Te 5*d* states are situated from 3.9 eV to 9.8 eV above the Fermi level. Although the Fe_1 and Fe_2 3*d* states situated between −6.6 eV and 4 eV energy interval are very similar, they still have some differences. There is a strong spin-down peak at −0.9 eV at the Fe_1 site, while the corresponding peak at the Fe_2 site is much weaker. Besides, the Fe_1 site possesses a quite intense spin-down peak just above the Fermi level, while a similar peak is much smaller at the Fe_2 site. Both the sites have quite large spin-down 3*d* density of states and small spin-up ones above the Fermi level.

TABLE I. On-site spin m_s and orbital m_l magnetic moment of two different Fe sites in Fe_3GeTe_2. The calculations are performed with the GGA approximation using the FLAPW and RLMTO methods, as well as the AMF and FLL schemes of PBE+*U*.

Bulk	*U*	*J*	Fe_1		Fe_2	
Method	(Ry)	(Ry)	m_s	m_l	m_s	m_l
FLAPW			2.36	0.07	1.55	0.03
RLMTO			1.91	0.12	1.26	0.02
sum rules			2.11	0.11	1.32	0.02
AMF	0.1		2.32	0.13	1.59	0.05
	0.2		1.77	0.14	1.65	0.08
FLL	0.1		2.62	0.08	1.81	0.07
	0.2		2.82	0.11	2.09	0.13
Exp[a]			2.18		1.54	
Film						
FLAPW			2.35	0.07	1.55	0.03
FLL	0.2	0.00	2.80	0.11	2.08	0.13
	0.2	0.10	2.60	0.12	1.84	0.12
	0.2	0.15	2.48	0.17	1.71	0.12

[a] Total magnetic moment measured using neutron powder diffraction by May *et al.* [59].

The on-site spin and orbital magnetic moments of both Fe sites in bulk and thin-film Fe_3GeTe_2, calculated using various methods, are listed in Table I and compared with the on-site total magnetic moments from neutron powder diffraction. Fe_1 has larger spin and orbital moments than Fe_2 does, which is consistent with published experimental and theoretical results [59, 60]. Within the GGA approximation, the calculated ratio between Fe_1 and Fe_2 total magnetic moments is equal to 1.54, which is larger than the experimental value of 1.45 [59] by about 10%. GGA underestimates the orbital moment by $\sim 40\%$, in comparison with the experimental value of $m_l = 0.10$ μ_B obtained using the XMCD [32]. However, the fully relativistic LMTO method produces an orbital magnetic moment in better agreement with the experiment (Table I).

We also present in the Table I the Fe spin and orbital magnetic moments obtained by the sum rules [Eqs. (3) and (4)] applied to the theoretically calculated XAS and XMCD spectra in the GGA approximation in a frame of the RLMTO method. Although the XMCD sum rules are derived within an ionic model using a number of approximations and the application of the sum rules sometimes results in an error up to 50% [40], we found relatively good agreement between the theoretically calculated magnetic moments and those derived from the sum rules.

Since DFT+*U* improves agreement between theoretical STM simulation and experimental STM images [61],

it is interesting to understand the correlation effects of $3d$ electrons in the Fe_3GeTe_2. To investigate the correlation effects on magnetism of Fe_3GeTe_2, we perform GGA+U calculations and checked if the on-site Coulomb interaction term U is able to improve agreement with experiments. The results depend on the double counting schemes used. Table I shows calculated magnetic moments with $U = 0.1$ and 0.2 Ry using both the AMF and FLL schemes. The orbital moments (m_l) in both schemes are increased with increasing U parameter, improving the agreement with the experiment. While, for the spin moments, the FLL scheme increases m_s on both sites, deviating further from experiments, the AMF scheme decreases (increases) m_s on Fe_1 (Fe_2) sites giving better agreement with the experiment. Thus, overall, a small U parameter within the AMF scheme improves the agreement with the experiment.

We also investigated the influence of Hunds's J parameter and the surface effects. The magnetic moments of the bulk and film are nearly identical, reflecting the van der Waals nature of the system. Table I also shows the dependence of the magnetic moments on the Hunds's J parameter in film Fe_3GeTe_2. With increasing of J values, spin moments are decreased at both iron sites while the orbital moment is increased only on the Fe_1 site. Thus the spin fluctuation introduced by Hund's J improves the agreement with experiments. Our work suggests that using a single value for the U parameter may not be sufficient for describing this system. An explicit treatment of electron correlations beyond DFT for these systems may be valuable [62, 63].

2. *The XAS and XMCD spectra*

Figure 3 presents the calculated XAS as well as XMCD spectra of the Fe_3GeTe_2 compound at the Fe $L_{3,2}$ edges in the GGA approximation compared with the experimental data [32]. The XMCD spectra at the Fe $L_{3,2}$ edges are mostly determined by the strength of the spin-orbit (SO) coupling of the initial Fe $2p$ core states and spin-polarization of the final empty $3d_{3/2,5/2}$ states while the exchange splitting of the Fe $2p$ core states as well as the SO coupling of the $3d$ valence states are of minor importance for the XMCD spectra at the Fe $L_{3,2}$ edges of Fe_3GeTe_2. Because of the dipole selection rules, apart from the $4s_{1/2}$ states (which have a small contribution to the XAS spectrum due to relatively small $2p \rightarrow 4s$ matrix elements) only $3d_{3/2}$ states occur as final states for L_2 XAS spectrum for unpolarized radiation, whereas for the L_3 XAS spectrum the $3d_{5/2}$ states also contribute. [40] Although the $2p_{3/2} \rightarrow 3d_{3/2}$ radial matrix elements are only slightly smaller than for the $2p_{3/2} \rightarrow 3d_{5/2}$ transitions the angular matrix elements strongly suppress the $2p_{3/2} \rightarrow 3d_{3/2}$ contribution [40]. Therefore neglecting the energy dependence of the radial matrix elements, the L_2 and the L_3 spectrum can be viewed as a direct mapping of the DOS curve for $3d_{3/2}$ and $3d_{5/2}$ character, respectively.

The experimental Fe L_3 XAS spectrum has one prominent peak around 708 eV and a pronounced shoulder of a peak at around 710 eV shifted by about 2 eV with respect to the maximum to higher photon energy. This structure is less pronounced at the L_2 edge spectrum. This result can be ascribed to the lifetime broadening effect because the lifetime of the $2p_{1/2}$ core hole is shorter than the $2p_{3/2}$ core hole due to the L_2L_3V Coster-Kronig decay. The GGA approximation reasonably well describes the shape of the XAS spectra at the Fe $L_{3,2}$ edges (the upper panel of Fig. 3), however it underestimates the high energy peak at around 710 eV. The calculated spectra have also smaller width compared to the experimental spectra.

The lower panel of the Fig. 3 shows XMCD spectra of the Fe_3GeTe_2 compound at the Fe $L_{3,2}$ edges in the GGA approximation compared with the experimental data [32]. The Fe_1 site shows stronger XMCD spectra than the Fe_2 site due to larger orbital magnetic moment at the Fe_1 site in comparison with the Fe_2 one.

We found minor influence of the final-state interaction on the shape of the Fe $L_{3,2}$ edges XAS and XMCD spectra in the whole energy interval (red curves in Fig. 3).

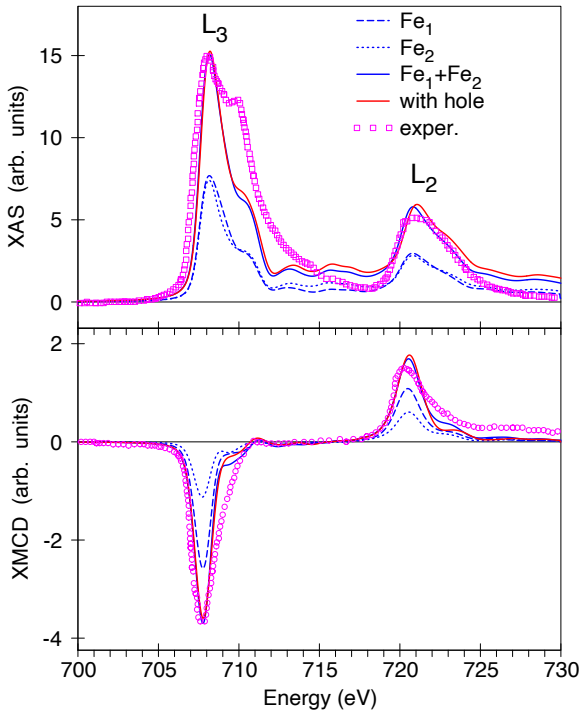

FIG. 3. Comparison of calculated Fe $L_{3,2}$-edges XAS and XMCD spectra of bulk Fe_3GeTe_2 with experiment. The solid red (blue) line is with (without) core-hole effects. The experimental data are obtained from Ref. [32].

Zhu *et al.* [32] compared total DOSs calculated by DFT and DFT+DMFT. Their DFT result shows a broad peak right above E_F and two sharp peaks at higher energies. However, in the DFT+DMFT calculation, the E_F

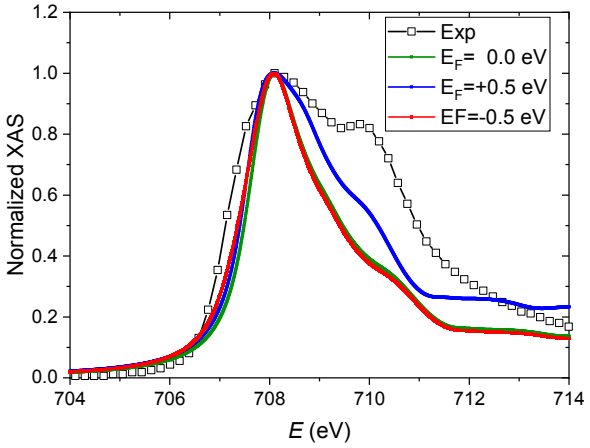

FIG. 4. Comparison of bulk XAS spectra at L_3 edge of Fe_3GeTe_2 with shifting E_F. The green is the spectral line shape with GGA and the blue (red) is the result that E_F is shifted 0.5eV up (down). The line with open squares is the experimental result [32].

is located at the peak which is much narrower than the DFT peak near E_F. It is possible that DFT overcounts down spin empty states just above E_F so that it overemphasizes the first peak of the XAS spectrum. To check this scenario, we calculated the spectrum with shifted E_F. Shifting E_F can mimic the change in the number of electrons and mimic doping. It is interesting to find the change of relative intensity between the two peaks with E_F changes. Figure 4 shows XAS spectra with the GGA functional and with $\pm 0.5\ eV$ shifted E_F from GGA results. As expected, shifting E_F up reduces unoccupied states of down spin and the intensity of the first peak of the spectra. It results in the second peak becoming relatively stronger than for the GGA result.

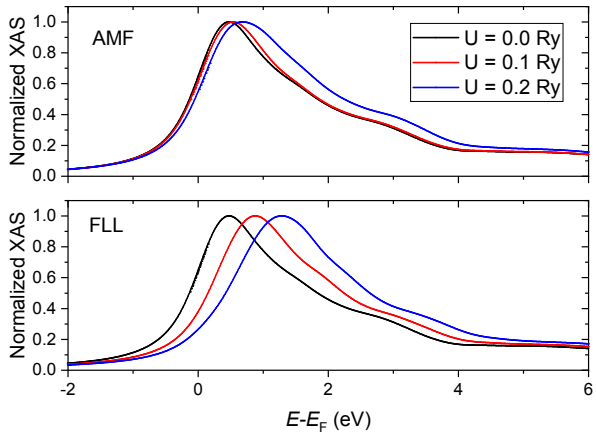

FIG. 5. Calculated Fe_3GeTe_2 bulk XAS spectra with different U values. The top (bottom) panel shows results of the AMF (FLL) scheme of the GGA+U method.

Since the XAS spectral line shape depends on details of DOS or band structure and an on-site Coulomb interaction changes electronic structure, it is interesting to find how the spectra change with different U values. We calculated the spectrum with the around mean field (AMF) and the fully localized limit (FLL) schemes of LDA+U to see how the spectra change with U and J values. The top panel of Fig. 5 shows results with the AMF scheme. As the figure shows, higher U values give broader XAS spectral shape and a relatively higher shoulder of the peak which is related to the lower spin moment (See Table I). The bottom panel of Fig. 5 shows results of the FLL scheme with $U = 0.1$ and $0.2\,\mathrm{Ry}$ but $J = 0\,\mathrm{eV}$. For XAS spectra, instead of getting a broader line shape, the main peaks are moving toward higher energy. With increasing J value, the XAS redtxspectrum is slightly shifted toward higher energy but the XMCD spectrum becomes narrower (not shown). Although there are changes in details of the spectra, overall spectral line shapes change little. The GGA+U method produces altered electronic structure compared to the GGA functional but the effects of U on the XAS (XMCD) spectral line shape are not significant.

B. CrI_3

1. *The electronic structure*

Figure 6 presents the partial density of states of CrI_3 in the GGA approximation. The $5p$ states of I are located in the -5.1 eV to 2.7 eV energy interval. It is interesting to note that the $5s$ partial DOS of I is extremely small and the number of the I $5s$ electrons is equal to 0.02 in CrI_3 instead of 2 in the free I atom. The Cr $3d$ spin up states are situated in the -5.1 eV and 1.5 eV energy interval. The empty Cr $3d$ spin-up DOS shows up as a single peak in the 0.7eV to 1.5 eV interval. The empty Cr $3d$ spin-down DOSs consist of two narrow intensive peaks in the 1.4 eV to 2.1 eV and 2.2 eV to 2.6 intervals, respectively.

Table II and Table III show calculated Cr magnetic moments and band gaps of bulk CrI_3 with various U and J-parameters. While the AMF scheme gives lower spin moment with increasing U parameters, the FLL scheme produces changes in the opposite direction. Gudelli *et al.* [64] performed GGA+U calculations for bulk, mono-,bi-, and tri-layer of CrI_3 and found the orbital moments are parallel to spin moments for the Cr atom. This agrees with the result that is presented here. However, the results that are estimated from XMCD spectra and atomic calculations [34, 35] are in the opposite direction compared to GGA and GGA+U results. The magnetic moment of Cr in a thin film is not so different from the bulk case (See Table S1 in Supplemental Material [65]). It is because the Cr atom layers are shielded by I atom layers. If Cr atoms are located on the top surface, they may acquire a larger moment but because of Van der Waals bonding character - the inter-layer interaction is much weaker than the intra-layer interaction, it

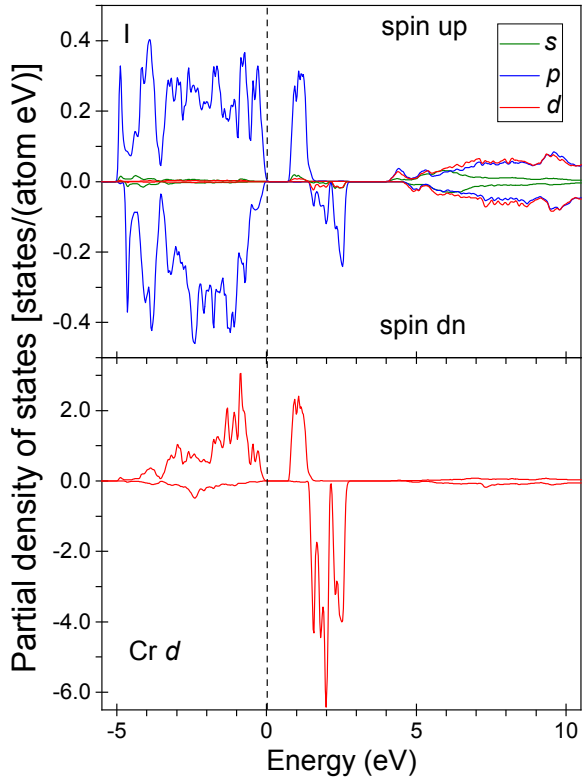

FIG. 6. The partial DOSs of bulk CrI_3 calculated in the GGA approximation.

is not plausible to obtain structures where Cr atoms are on the top surface.

TABLE II. On-site spin m_s and orbital m_l magnetic moments of Cr of CrI_3. FLL is calculated with $J = 0$ Ry. Experimental orbital moments are obtained by XMCD measurement.

CrI_3	U	Cr		gap
Method	Ry	m_s	m_l	eV
FLAPW		2.99	0.074	0.77
RLMTO		3.23	0.118	0.42
sum rules		2.74	0.108	
AMF	0.1	2.84	0.078	1.06
	0.2	2.63	0.080	1.31
	0.4	2.12	0.074	0.72
FLL	0.1	3.17	0.070	0.74
	0.2	3.22	0.068	0.72
	0.4	3.42	0.062	0.65
Exp [35]			-0.059	

2. *The XAS and XMCD spectra*

Figure 7 shows calculated XAS and XMCD spectra with GGA functionals. The left (right) panel shows L_3 (L_2)-edge spectra. Both XASs show three structures : a peak around 1 eV, a central peak around 1.9 eV and a shoulder of a peak around 2.4 eV. XMCD spectra also have three features - the first has a different sign compared to the other two peaks.

TABLE III. U and J dependency of on-site spin m_s and orbital m_l magnetic moment of Cr of CrI_3

CrI_3	J	Cr		gap
U (Ry)	Ry	m_s	m_l	eV
0.30	0.05	3.14	0.066	0.90
	0.10	2.85	0.065	1.30
	0.20	2.15	0.055	0.68
0.40	0.05	3.17	0.062	0.86
	0.10	3.22	0.061	1.29
	0.20	3.42	0.062	0.60

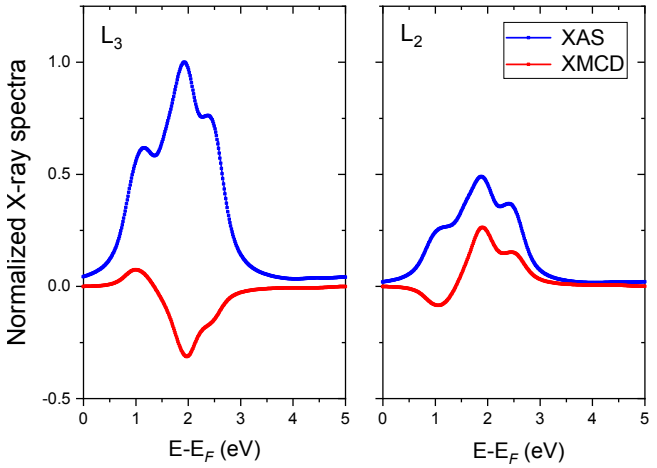

FIG. 7. Calculated L_3 (left panel) and L_2 (right panel) edge XAS (blue) and XMCD (red) spectra in bulk CrI_3. The GGA functional was employed for the calculation. Each spectrum shows three structures.

Frisk *et al.*'s [34] measured L_3 edge XAS spectrum shows a strong peak around 576 eV photon energy and shoulders on both sides of the central peak. However, their calculated spectra does not show the shoulder at higher energy but a smooth decreasing from the central peak. With these results, they suggested that the higher energy shoulder is attributed to partial oxidation. Kim *et al.*'s [35] results look similar to Frisk *et al.*'s except for the shoulder at higher energy. They observed a small shoulder-like peak and were able to reproduce it by their model calculation. It seems that the third peak is intrinsic and small, although it can be intensified by oxidation.

The top panel of Fig. 8 shows Cr L_3-edge XAS spectrum which was calculated using radial matrix elements and DOS. It not only reproduces the three features of Fig. 7 well but also gives more information on the character of the peaks if it is combined with DOS (the bottom panel of Fig. 8). The spectrum was decomposed into up

spin (red) and down spin (blue) contributions. It shows the first peak is attributed to the up spin state and the other two peaks are from the down spin state. It also explains why the first peak of the XMCD spectrum has the opposite sign of the other two peaks.

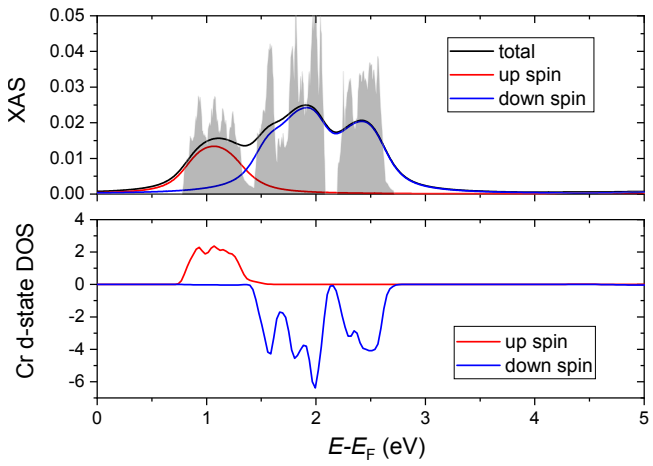

FIG. 8. The top panel shows CrI_3 bulk L_3-edge XAS spectrum which was calculated by $\mu_{xas} = M^{\uparrow 2}(E)\rho^{\uparrow}(E) + M^{\downarrow 2}(E)\rho^{\downarrow}(E)$. where M and ρ is radial matrix elements and density of state respectively. Red (blue) line presents up (down) spin contribution and the shadow region show no broadening effects. The bottom panel shows spin-decomposed Cr d-state DOS of CrI_3. See Fig. S2 in Supplemental Material [65] for the spin dependent radial matrix elements of CrI_3.

The main difference between the measured XAS and the calculated XAS spectra with GGA is the spectral width. The calculated spectra have much narrower spectral widths than the experimental results. The spectral intensity of the calculated spectra is rapidly decreased after the third peak. It is because Cr $3d$ bandwidth is narrow and the top of the band is located about 2.5 eV from E_F which corresponds to about 576.6 eV. The sign of the calculated XMCD peaks is also not consistent with the experiment. While the experimental result shows a negative sign for the first and second peaks and a positive sign for the third peak, the calculated spectra show a positive sign for the first peak and negative for the others.

The XMCD spectrum depends on details of m_l decomposed DOS. The GGA+U method is able to adjust relative positions of m_l decomposed DOS by controlling U values. Therefore, it is possible to tune the calculated spectra by using different U values. We have performed the GGA+U calculations to understand the effects of U and J values on X-ray spectra and to check if the GGA+U method is able to produce X-ray spectra that are consistent with the experimental results.

Figure 9 shows the result with $U = 0.4\,\mathrm{Ry}$ (See Fig. S3 for a lower U value result). For a comparison, it also includes experimental data that are obtained from Frisk *et al.* [34]. Since higher U parameters promote $3d$ band splittings to be stronger and band widths to be wider, the

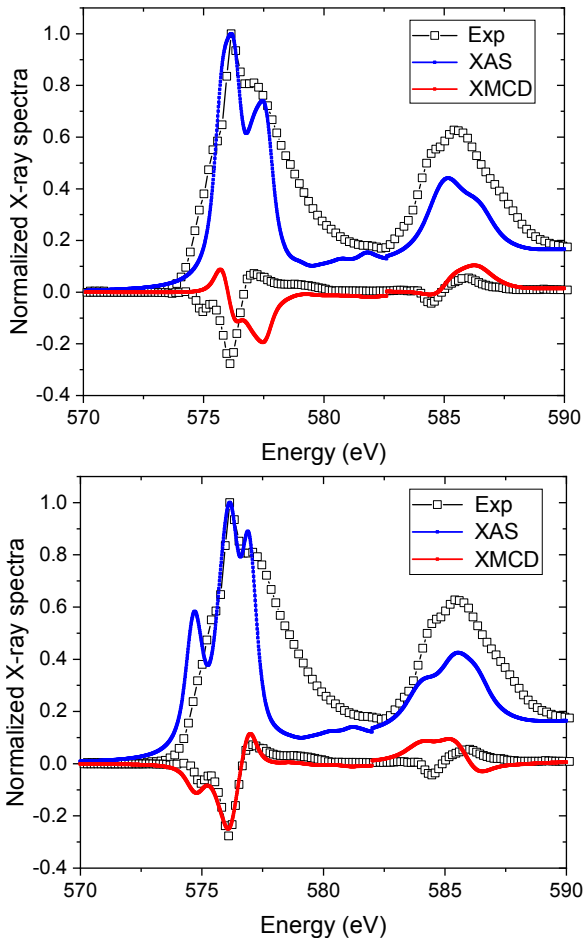

FIG. 9. Calculated CrI_3 bulk L_3 and L_2-edge XAS (blue lines)and XMCD (red lines) spectra. The top panel shows results of FLL scheme with $U = 0.4\,\mathrm{Ry}$ and $J = 0.1\,\mathrm{Ry}$. The bottom panel shows AMF scheme results with $U = 0.4\,\mathrm{Ry}$. The lines with open squares are experimental data which were obtained from Frisk *et al.* [34].

calculated spectra have wider spectral widths. For the XAS spectra, the AMF scheme gives better agreement with experiment than the FLL scheme. The calculation with the AMF scheme gives good agreement with the experiment for the L_3-edge but not for the L_2-edge XMCD spectrum. It is reversed from the calculation with the FLL scheme. The calculated XMCD spectrum with the FLL scheme shows reasonable agreement for the L_2-edge but not for the L_3-edge.

The normalized X-ray spectra of the thin film are similar to the spectra of the bulk CrI_3 except for details of fine structure of the L_3-edge XAS spectrum. See Fig. S4 in Supplemental Material [65] for X-ray spectra of the film. The FLL scheme with $U = 0.4\,\mathrm{Ry}$ and $J = 0.1\,\mathrm{Ry}$ is able to reproduce most of the experimental features except for the higher energy peak (around 576.6 eV photon energy) of L_3-edge XMCD spectrum. While the AMF scheme with $U = 0.4\,\mathrm{Ry}$ produces the L_3-edge XMCD spectrum which shows good agreement with the experimental re-

sult, it flips of the sign of lower energy peak of the L_2-edge XMCD spectrum. For the L_3 edge XMCD spectrum, the lowest energy peak which has a positive sign is attributed to the up spin state and the other two peaks which have negative signs are attributed to the down spin state. The positive peak is located at the highest energy in the L_3 edge XMCD spectrum calculated by the AMF scheme.

Overall, the GGA+U method is able to improve theoretical spectra of the bulk CrI_3 but it requires a rather higher U value. The results with $U \approx 5.2$ eV show good agreement with the measured spectra but this U is much higher than the values from published work. For instance, the employed U values are 1.0 eV in Gudelli *et al.* [64], 2.0, 2.9 eV in Jang *et al.*'s [9], and 3.0 eV in Sivadas *et al.* [66].

C. $CrGeTe_3$

1. *The electronic structure*

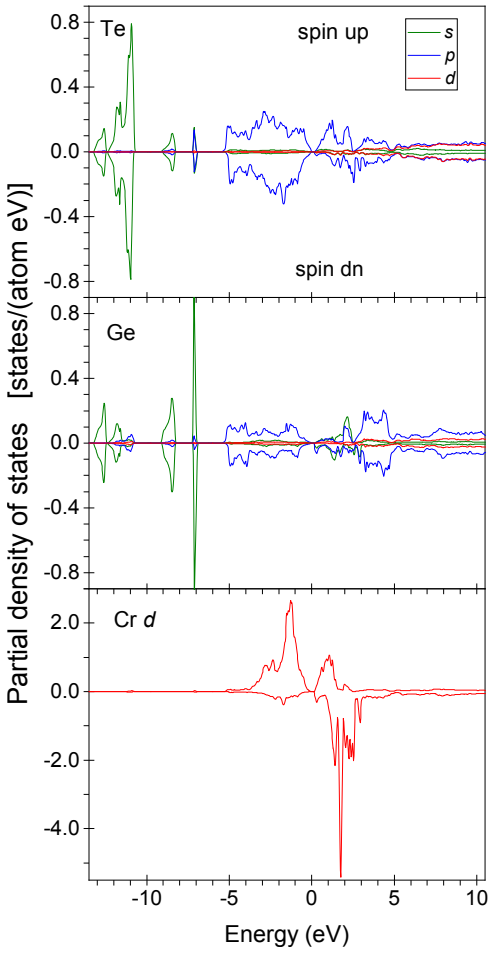

FIG. 10. The partial DOS of bulk $CrGeTe_3$ calculated in the GGA approximation.

Figure 10 presents the partial density of states of $CrGeTe_3$ in the GGA approximation. The Te 5s states consist of four peaks and they are located mostly between -12.2 and -10.7 eV below the Fermi level. The Ge 4s states are located mostly between -7.2 and -7 eV. Other peaks located at the lower energy originate from the hybridization with Te 5s states. The 5p states of Te and Ge are found in the at -5.5 eV to 5.0 eV energy interval in $CrGeTe_3$. The spin splitting of the Te and Ge p states is quite small. The Cr 3d states are situated in the -5 eV to 3.2 eV energy interval. The empty Cr 3d spin-up DOSs present a relatively weak peak in the 0 eV to 1.3 eV interval. The empty Cr 3d spin-down DOSs consist of three intensive peaks in the 0.5 eV to 3.2 eV interval.

Table IV summarizes calculated spin, orbital magnetic moment and band-gap size. The trend of magnetic moment change with U-parameter is similar to the trend in the CrI_3 case. While the spin moment is decreasing with increasing U-parameter in the AMF scheme, it changes to the opposite direction in the FLL scheme. The calculated orbital moments in the Table IV are too small to assign physical meaning though the value is getting more negative with increasing U value. The measured saturated magnetization is 2.92 μ_B at 5 K [56] and the orbital moment is $-0.045\,\mu_B$ [35]. Calculated orbital moment with GGA+U is much smaller than the measured result.

TABLE IV. On-site spin m_s and orbital m_l magnetic moment of Cr of $CrGeTe_3$ bulk. For the FLL scheme calculation, the site exchange J is set to be 0 Ry.

$CrGeTe_3$	U	Cr		gap
Method	Ry	m_s	m_l	eV
FLAPW		3.06	0.004	0.18
RLMTO		3.34	0.029	0.00
sum rules		3.27	0.031	
AMF	0.10	2.91	0.003	0.15
	0.20	2.65	0.002	0.08
	0.40	1.93	-0.003	0.00
FLL	0.10	3.21	0.001	0.14
	0.20	3.36	-0.001	0.08
	0.40	3.60	-0.003	0.00
Exp [35]			-0.045	

2. *The XAS and XMCD spectra*

Figure 11 shows calculated XAS and XMCD spectra with GGA functional. The left panel is Cr-L_3-edge spectra and the right panel is Cr L_2-edge spectra. Both XAS spectra show three features which are a strong central peak around 1.8 eV, and two shallow shoulders on both sides of the central peak around 1.2 eV and 2.3 eV. Since the distances between peaks are rather close, the spectra look like a broad peak unlike the Cr XAS spectra of CrI_3 which show separated peaks.

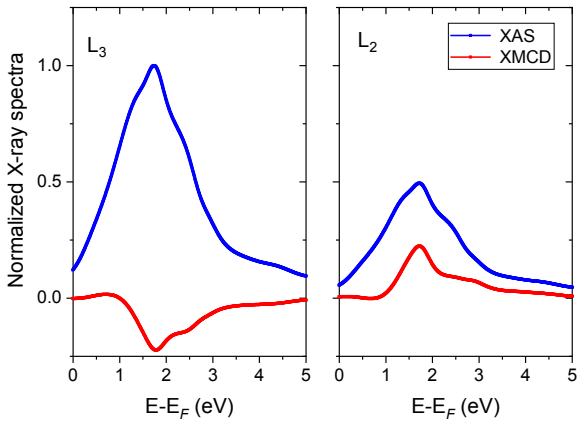

FIG. 11. Calculated bulk $CrGeTe_3$ XAS (blue line) and XMCD (red line) spectra with the GGA functional. Left(Right) panel shows Cr L_3 (L_2)-edge spectra.

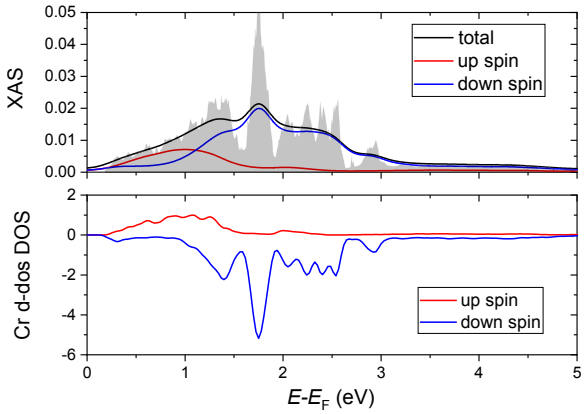

FIG. 12. Cr L_3 edge XAS spectrum of $CrGeTe_3$ (top panel) and spin resolved DOS (bottom panel). Red(Blue) line is up(down) spin contribution. The shadow area presents raw spectra.

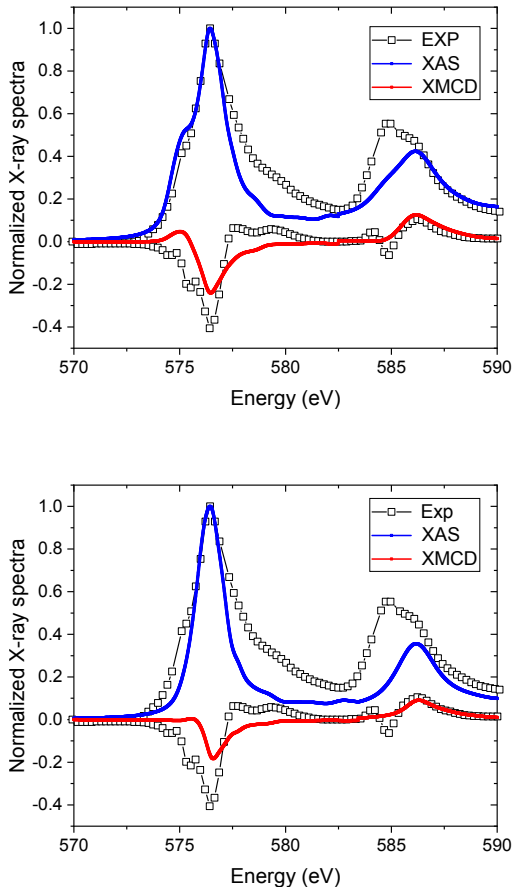

FIG. 13. Comparison between calculated and measured Cr L_3 and L_2-edge XAS and XMCD spectra of $CrGeTe_3$. The calculation was performed with the GGA+U method. The employed U value was 0.1 Ry for both the FLL and the AMF scheme. The top (bottom) panel show the result with FLL (AMF) scheme. The blue (red) line is theoretical XAS (XMCD) spectra. Experimental data (open squares) were obtained from Kim *et al.* [35].

The top panel of Fig. 12 shows Cr L_3 XAS spectrum which is calculated by using radial matrix elements and the Cr d-state DOS. It clearly shows that all three features of the XAS spectrum are attributed to the down spin DOS. The bottom panel shows the Cr d-state DOS which has a broader bandwidth than Cr d-state of CrI_3. It suggests that the Cr atom in $CrGeTe_3$ is involved in stronger hybridization than in CrI_3. In their atomic calculations of XAS/XMCD spectra of $CrGeTe_3$, Watson *et al.* [36] observed that a strong hybridization parameter is required to obtain results that show good agreement with the experimental result. Menichetti *et al.* [67] also reported that increasing the applied U potential decreases the band-gap and attributed it to strong hybridization between the Cr and Te atoms.

Figure 13 shows the calculated spectra with the FLL(top panel) and the AMF(bottom panel) schemes of the GGA+U method. The top panel shows that two lower energy peaks are separated further compared to Fig. 11. Although the L_3-edge of the XAS spectrum, which is calculated using the FLL scheme, shows good agreement with the experiment, overall agreement between theoretical and experimental spectra is not so good. Using a higher U value does not improve the agreement. It seems that the Hubbard U is less effective for the Cr atom in the $CrGeTe_3$ than in the CrI_3 since the Cr atom in the $CrGeTe_3$ is involved in stronger hybridization.

IV. CONCLUSION

We performed first principles electronic structure calculations for bulk and thin film structures of m2DvdW

materials Fe_3GeTe_2, CrI_3 and $CrGeTe_3$ with the GGA functional and the GGA+U methods. XAS, XMCD spectra were calculated using wavefunctions that were generated by first principles calculations. We show that the GGA is applicable for the metallic Fe_3GeTe_2 and the GGA+U method with a rather higher U value is required for the semiconducting CrI_3. Although $CrGeTe_3$ is a semiconductor, because of the strong hybridization between Cr and Te atom, the spectral line shapes are not so sensitive to the values of the Hubbard U. The core-hole effects are not so strong to alter the spectral line shapes.

Our calculations comparing experimental X-ray spectra and detailed calculations including theoretical density of states (DOS) help to clarify the various contributions to specific features of the experimental X-ray $L_{3,2}$-edges spectra. Comparing to Cr compounds, Fe_3GeTe_2 shows broader width for the XAS $L_{3,2}$ spectra, since it has broader $3d$ bandwidth. The XMCD $L_{3,2}$ spectra show strong Fe sites dependence unlike the XAS spectra. The spectra shape for CrI_3 is characterized by the three narrow unoccupied bands giving rise to strong peaks (one for up spin and two for down spin).

Our calculations have demonstrated that DFT and DFT+U methods are very useful for understanding rather complex experimental X-ray spectra; however our results (Fe_3GeTe_2 and $CrGeTe_3$) clearly point to areas where more sophisticated methods are required to improve agreement with some experiments. It is important to establish these deficiencies so that more complete and accurate theoretical methods can be formulated and applied.

ACKNOWLEDGMENTS

This work was supported by the U.S. Department of Energy, Office of Science, Office of Basic Energy Sciences, Materials Sciences and Engineering Division, and Early Career Research Program. Ames Laboratory is operated for the U.S. Department of Energy by Iowa State University under Contract No. DE-AC02-07CH11358.

[1] M. J. Allen, V. C. Tung, and R. B. Kaner, Honeycomb Carbon: A Review of Graphene, Chemical Reviews **110**, 132 (2010).

[2] W. Choi, I. Lahiri, R. Seelaboyina, and Y. S. Kang, Synthesis of Graphene and Its Applications: A Review, Critical Reviews in Solid State and Materials Sciences **35**, 52 (2010).

[3] M. Acik and Y. J. Chabal, Japan Society of Applied Physics **50**, 070101 (2011).

[4] M. Coros, F. Pogacean, L. Magerusan, C. Socaci, and S. Pruneanu, A brief overview on synthesis and applications of graphene and graphene-based nanomaterials, Frontiers of Materials Science **13**, 23 (2019).

[5] O. V. Yazyev and M. Katsnelson, Theory of Magnetism in Graphene, in *Advanced Functional Materials*, Science and Technology of Atomic, Molecular, Condensed Matter & Biological Systems, Vol. 2, edited by T. P. Das, B. Sanyal, and O. Eriksson (Elsevier, 2012) pp. 71 – 103.

[6] E. Kan, Z. Li, and J. Yang, Magnetism in graphene systems, Nano **03**, 433 (2008).

[7] C. Gong, L. Li, Z. Li, H. Ji, A. Stern, Y. Xia, T. Cao, W. Bao, C. Wang, Y. Wang, Z. Q. Qiu, R. J. Cava, S. G. Louie, J. Xia, and X. Zhang, Discovery of intrinsic ferromagnetism in two-dimensional van der Waals crystals, Nature **546**, 265 (2017).

[8] B. Huang, G. Clark, E. Navarro-Moratalla, D. R. Klein, R. Cheng, K. L. Seyler, D. Zhong, E. Schmidgall, M. A. McGuire, D. H. Cobden, W. Yao, D. Xiao, P. Jarillo-Herrero, and X. Xu, Layer-dependent ferromagnetism in a van der waals crystal down to the monolayer limit, Nature **546**, 270 (2017), letter.

[9] S. W. Jang, M. Y. Jeong, H. Yoon, S. Ryee, and M. J. Han, Microscopic understanding of magnetic interactions in bilayer cri_3, Physical Review Materials **3**, 031001 (2019).

[10] J. L. Lado and J. Fernández-Rossier, On the origin of magnetic anisotropy in two dimensional CrI3, 2D Materials **4**, 035002 (2017).

[11] T. Li, S. Jiang, N. Sivadas, Z. Wang, Y. Xu, D. Weber, J. E. Goldberger, K. Watanabe, T. Taniguchi, C. J. Fennie, K. Fai Mak, and J. Shan, Pressure-controlled interlayer magnetism in atomically thin cri3, Nature Materials **18**, 1303 (2019).

[12] F. Subhan, I. Khan, and J. Hong, Pressure-induced ferromagnetism and enhanced perpendicular magnetic anisotropy of bilayer CrI3, Journal of Physics: Condensed Matter **31**, 355001 (2019).

[13] S. Mondal, M. Kannan, M. Das, L. Govindaraj, R. Singha, B. Satpati, S. Arumugam, and P. Mandal, Effect of hydrostatic pressure on ferromagnetism in two-dimensional cri_3, Phys. Rev. B **99**, 180407 (2019).

[14] S. Jiang, L. Li, Z. Wang, K. F. Mak, and J. Shan, Controlling magnetism in 2d cri3 by electrostatic doping, Nature Nanotechnology **13**, 549 (2018).

[15] H. Wang, F. Fan, S. Zhu, and H. Wu, Doping enhanced ferromagnetism and induced half-metallicity in CrI_3 monolayer, EPL (Europhysics Letters) **114**, 47001 (2016).

[16] Q.-F. Xu, W.-Q. Xie, Z.-W. Lu, and Y.-J. Zhao, Theoretical study of enhanced ferromagnetism and tunable magnetic anisotropy of monolayer cri3 by surface adsorption, Physics Letters A **384**, 126754 (2020).

[17] E. S. Morell, A. León, R. H. Miwa, and P. Vargas, Control of magnetism in bilayer CrI 3 by an external electric field, 2D Materials **6**, 025020 (2019).

[18] I. uti, A. Matos-Abiague, B. Scharf, H. Dery, and K. Belashchenko, Proximitized materials, Materials Today **22**, 85 (2019).

[19] Y. Liu, Y. Huang, and X. Duan, Van der Waals integration before and beyond two-dimensional materials, Na-

ture **567**, 323 (2019).
[20] J. Kang, S. Tongay, J. Zhou, J. Li, and J. Wu, Band offsets and heterostructures of two-dimensional semiconductors, Applied Physics Letters **102**, 012111 (2013).
[21] J. Shang, X. Tang, X. Tan, A. Du, T. Liao, S. C. Smith, Y. Gu, C. Li, and L. Kou, Stacking-Dependent Interlayer Magnetic Coupling in 2D CrI_3/$CrGeTe_3$ Nanostructures for Spintronics, ACS Applied Nano Materials **3**, 1282 (2020).
[22] J.-F. Dayen, S. J. Ray, O. Karis, I. J. Vera-Marun, and M. V. Kamalakar, Two-dimensional van der Waals spinterfaces and magnetic-interfaces, Applied Physics Reviews **7**, 011303 (2020).
[23] M. Gibertini, M. Koperski, A. F. Morpurgo, and K. S. Novoselov, Magnetic 2D materials and heterostructures, Nature Nanotechnology **14**, 408 (2019).
[24] Z. Shi, X. Wang, Y. Sun, Y. Li, and L. Zhang, Interlayer coupling in two-dimensional semiconductor materials, Semiconductor Science and Technology **33**, 093001 (2018).
[25] S. Liu, K. Yang, W. Liu, E. Zhang, Z. Li, X. Zhang, Z. Liao, W. Zhang, J. Sun, Y. Yang, H. Gao, C. Huang, L. Ai, P. K. J. Wong, A. T. S. Wee, A. T. NDiaye, S. A. Morton, X. Kou, J. Zou, Y. Xu, H. Wu, and F. Xiu, Two-dimensional ferromagnetic superlattices, National Science Review (2019).
[26] D. M. Burn, L. B. Duffy, R. Fujita, S. L. Zhang, A. I. Figueroa, J. Herrero-Martin, G. van der Laan, and T. Hesjedal, Cr_2Te_3 Thin Films for Integration in Magnetic Topological Insulator Heterostructures, Scientific Reports **9**, 10793 (2019).
[27] J. Stöhr and H. Siegmann, *Magnetism: From Fundamentals to Nanoscale Dynamics*, Springer Series in Solid-State Sciences (Springer, 2006).
[28] H. Wende, Recent advances in x-ray absorption spectroscopy, Reports on Progress in Physics **67**, 2105 (2004).
[29] W. Zhang, P. K. J. Wong, X. Zhou, A. Rath, Z. Huang, H. Wang, S. A. Morton, J. Yuan, L. Zhang, R. Chua, S. Zeng, E. Liu, F. Xu, Ariando, D. H. C. Chua, Y. P. Feng, G. van der Laan, S. J. Pennycook, Y. Zhai, and A. T. S. Wee, Ferromagnet/Two-Dimensional Semiconducting Transition-Metal Dichalcogenide Interface with Perpendicular Magnetic Anisotropy, ACS Nano **13**, 2253 (2019).
[30] C. Aruta, G. Ghiringhelli, V. Bisogni, L. Braicovich, N. B. Brookes, A. Tebano, and G. Balestrino, Orbital occupation, atomic moments, and magnetic ordering at interfaces of manganite thin films, Phys. Rev. B **80**, 014431 (2009).
[31] P. Srivastava, F. Wilhelm, A. Ney, M. Farle, H. Wende, N. Haack, G. Ceballos, and K. Baberschke, Magnetic moments and Curie temperatures of Ni and Co thin films and coupled trilayers, Phys. Rev. B **58**, 5701 (1998).
[32] J.-X. Zhu, M. Janoschek, D. S. Chaves, J. C. Cezar, T. Durakiewicz, F. Ronning, Y. Sassa, M. Mansson, B. L. Scott, N. Wakeham, E. D. Bauer, and J. D. Thompson, Electronic correlation and magnetism in the ferromagnetic metal Fe_3GeTe_2, Phys. Rev. B **93**, 144404 (2016).
[33] S. Y. Park, D. S. Kim, Y. Liu, J. Hwang, Y. Kim, W. Kim, J.-Y. Kim, C. Petrovic, C. Hwang, S.-K. Mo, H.-j. Kim, B.-C. Min, H. C. Koo, J. Chang, C. Jang, J. W. Choi, and H. Ryu, Controlling the magnetic anisotropy of the van der waals ferromagnet fe_3gete_2 through hole doping, Nano Letters **20**, 95 (2020).
[34] A. Frisk, L. B. Duffy, S. Zhang, G. [van der Laan], and T. Hesjedal, Magnetic X-ray spectroscopy of two-dimensional CrI_3 layers, Materials Letters **232**, 5 (2018).
[35] D.-H. Kim, K. Kim, K.-T. Ko, J. Seo, J. S. Kim, T.-H. Jang, Y. Kim, J.-Y. Kim, S.-W. Cheong, and J.-H. Park, Giant Magnetic Anisotropy Induced by Ligand LS Coupling in Layered Cr Compounds, Phys. Rev. Lett. **122**, 207201 (2019).
[36] M. D. Watson, I. Marković, F. Mazzola, A. Rajan, E. A. Morales, D. M. Burn, T. Hesjedal, G. van der Laan, S. Mukherjee, T. K. Kim, C. Bigi, I. Vobornik, M. Ciomaga Hatnean, G. Balakrishnan, and P. D. C. King, Direct observation of the energy gain underpinning ferromagnetic superexchange in the electronic structure of $CrGeTe_3$, Phys. Rev. B **101**, 205125 (2020).
[37] Q. Li, M. Yang, C. Gong, R. V. Chopdekar, A. T. NDiaye, J. Turner, G. Chen, A. Scholl, P. Shafer, E. Arenholz, A. K. Schmid, S. Wang, K. Liu, N. Gao, A. S. Admasu, S.-W. Cheong, C. Hwang, J. Li, F. Wang, X. Zhang, and Z. Qiu, Patterning-Induced Ferromagnetism of Fe_3GeTe_2 van der Waals Materials beyond Room Temperature, Nano Letters **18**, 5974 (2018).
[38] B. T. Thole, G. van der Laan, J. C. Fuggle, G. A. Sawatzky, R. C. Karnatak, and J.-M. Esteva, 3d x-ray-absorption lines and the $3d^9 4f^{n+1}$ multiplets of the lanthanides, Phys. Rev. B **32**, 5107 (1985).
[39] F. De Groot and A. Kotani, *Core Level Spectroscopy of Solids*, Advances in Condensed Matter Science (Taylor & Francis Group, 2008).
[40] V. Antonov, B. Harmon, and A. Yaresko, *Electronic Structure and Magneto-Optical Properties of Solids* (Kluwer, Dordrecht, 2004).
[41] B. T. Thole and G. van der Laan, Branching ratio in x-ray absorption spectroscopy, Phys. Rev. B **38**, 3158 (1988).
[42] B. T. Thole, P. Carra, F. Sette, and G. van der Laan, X-ray circular dichroism as a probe of orbital magnetization, Phys. Rev. Lett. **68**, 1943 (1992).
[43] P. Carra, B. T. Thole, M. Altarelli, and X. Wang, X-ray circular dichroism and local magnetic fields, Phys. Rev. Lett. **70**, 694 (1993).
[44] G. van der Laan and B. T. Thole, X-ray-absorption sum rules in jj-coupled operators and ground-state moments of actinide ions, Phys. Rev. B **53**, 14458 (1996).
[45] L. Pardini, V. Bellini, F. Manghi, and C. Ambrosch-Draxl, First-principles calculation of X-ray dichroic spectra within the full-potential linearized augmented planewave method: An implementation into the WIEN2K code, Computer Physics Communications **183**, 628 (2012).
[46] P. Blaha, K. Schwarz, F. Tran, R. Laskowski, G. K. H. Madsen, and L. D. Marks, WIEN2K: An APW+lo program for calculating the properties of solids, Journal of Chemical Physics **152**, 074101 (2020).
[47] O. K. Andersen, Linear methods in band theory, Phys. Rev. B **12**, 3060 (1975).
[48] A. Y. Perlov, A. N. Yaresko, and V. N. Antonov, PY-LMTO, A Spin-polarized Relativistic Linear Muffin-tin Orbitals Package for Electronic Structure Calculations (1995, unpublished).
[49] V. V. Nemoshkalenko, A. E. Krasovskii, V. N. Antonov, V. N. Antonov, U. Fleck, H. Wonn, and P. Ziesche, The relativistic linear muffin-tin orbital method application to au, physica status solidi (b) **120**, 283 (1983).

[50] J. P. Perdew, K. Burke, and M. Ernzerhof, Generalized gradient approximation made simple, Phys. Rev. Lett. **77**, 3865 (1996).

[51] A. I. Liechtenstein, V. I. Anisimov, and J. Zaanen, Density-functional theory and strong interactions: Orbital ordering in mott-hubbard insulators, Phys. Rev. B **52**, R5467 (1995).

[52] V. I. Anisimov, I. V. Solovyev, M. A. Korotin, M. T. Czyżyk, and G. A. Sawatzky, Density-functional theory and NiO photoemission spectra, Phys. Rev. B **48**, 16929 (1993).

[53] M. T. Czyżyk and G. A. Sawatzky, Local-density functional and on-site correlations: The electronic structure of La_2CuO_4 and $LaCuO_3$, Phys. Rev. B **49**, 14211 (1994).

[54] A. N. Yaresko, V. N. Antonov, and P. Fulde, Localized u 5f electrons in upd3 from lda+u calculations, Phys. Rev. B **67**, 155103 (2003).

[55] M. A. McGuire, H. Dixit, V. R. Cooper, and B. C. Sales, Coupling of crystal structure and magnetism in the layered, ferromagnetic insulator CrI_3, Chemistry of Materials **27**, 612 (2015).

[56] V. Carteaux, D. Brunet, G. Ouvrard, and G. Andre, Crystallographic, magnetic and electronic structures of a new layered ferromagnetic compound $Cr_2Ge_2Te_6$, Journal of Physics: Condensed Matter **7**, 69 (1995).

[57] H.-J. Deiseroth, K. Aleksandrov, C. Reiner, L. Kienle, and R. K. Kremer, Fe_3GeTe_2 and Ni_3GeTe_2 Two New Layered Transition-Metal Compounds: Crystal Structures, HRTEM Investigations, and Magnetic and Electrical Properties, European Journal of Inorganic Chemistry **2006**, 1561 (2006).

[58] A. Kokalj, XCrySDena new program for displaying crystalline structures and electron densities, Journal of Molecular Graphics and Modelling **17**, 176 (1999).

[59] A. F. May, S. Calder, C. Cantoni, H. Cao, and M. A. McGuire, Magnetic structure and phase stability of the van der Waals bonded ferromagnet $Fe_{3-x}GeTe_2$, Phys. Rev. B **93**, 014411 (2016).

[60] V. Y. Verchenko, A. A. Tsirlin, A. V. Sobolev, I. A. Presniakov, and A. V. Shevelkov, Ferromagnetic Order, Strong Magnetocrystalline Anisotropy, and Magnetocaloric Effect in the Layered Telluride $Fe_{3-\delta}GeTe_2$, Inorganic Chemistry **54**, 8598 (2015).

[61] X. Kong, G. D. Nguyen, J. Lee, C. Lee, S. Calder, A. F. May, Z. Gai, A.-P. Li, L. Liang, and T. Berlijn, Interlayer magnetism in $fe_{3-x}gete_2$, Phys. Rev. Materials **4**, 094403 (2020).

[62] Y. Lee, T. Kotani, and L. Ke, Role of nonlocality in exchange correlation for magnetic two-dimensional van der Waals materials, Phys. Rev. B **101**, 241409 (2020).

[63] L. Ke and M. I. Katsnelson, Electron correlation effects on exchange interactions and spin excitations in 2D van der Waals materials, npj Computational Materials **7**, 1 (2021).

[64] V. K. Gudelli and G.-Y. Guo, Magnetism and magneto-optical effects in bulk and few-layer CrI3: a theoretical GGA+U study, New Journal of Physics **21**, 053012 (2019).

[65] See Supplemental Material for more detailed methods and additional results.

[66] N. Sivadas, S. Okamoto, X. Xu, C. J. Fennie, and D. Xiao, Stacking-Dependent Magnetism in Bilayer CrI_3, Nano Letters **18**, 7658 (2018).

[67] G. Menichetti, M. Calandra, and M. Polini, Electronic structure and magnetic properties of few-layer $Cr_2Ge_2Te_6$: the key role of nonlocal electron–electron interaction effects, 2D Materials **6**, 045042 (2019).